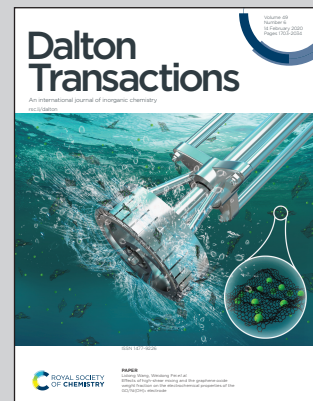


Showcasing research from the group of Prof. Chia-Ying Chiang's lab at National Taiwan University of Science and Technology.

Anion-induced morphological regulation of cupric oxide nanostructures and their application as co-catalysts for solar water splitting

A new strategy for simultaneously preparing and modulating the morphological structure evolution of copper layered hydroxyl salts and oxides is introduced by regulating the species of the presenting anions in the electroplating solution.

As featured in:



See Chia-Ying Chiang *et al.*, *Dalton Trans.*, 2020, **49**, 1765.



Cite this: *Dalton Trans.*, 2020, **49**, 1765

Anion-induced morphological regulation of cupric oxide nanostructures and their application as co-catalysts for solar water splitting†

Truong-Giang Vo, Shu-Ju Chang and Chia-Ying Chiang *
Published on 22 January 2020. Downloaded on 2/14/2020 4:20:53 AM.

Morphological control of nanomaterials is essential for their properties and potential applications, and many strategies have been developed. In this work, a new strategy for simultaneously preparing and modulating the morphological structure evolution of copper layered hydroxyl salts and oxides is introduced. By changing the nature of the anions in the electroplating solution, significant variations in the size and porosity of nanosheets are achieved. Porous CuO nanosheets with a higher surface area were obtained by the use of copper nitrate as a copper source, while CuO nanoflakes were produced from copper sulfate. Photoanodes combining these porous CuO nanomaterials and a typical light absorber (BiVO_4) exhibited good morphology-dependent activities for photoelectrochemical water splitting. The composite electrode displays a negative shift of 180 mV for the onset potential and an approximately 2-fold enhancement in the photocurrent compared to the bare BiVO_4 . The charge recombination rate in the photoelectrode with the porous CuO nanosheets was significantly lower than the bare photoanode due to the favorable electron diffusion path and effective charge collection. This research offers an effective method for constructing a highly active photoelectrocatalytic system for overall water splitting.

Received 4th December 2019,
Accepted 22nd January 2020

DOI: 10.1039/c9dt04626g

rsc.li/dalton

Introduction

Copper oxide-based materials have been widely studied with renewed interest over the past decade for diverse applications including supercapacitors,^{1,2} electrochemical sensors,^{3–5} lithium-ion electrode materials^{6–8} or heterogeneous catalysts.⁹ More recently, they have been demonstrated to electrocatalytically oxidize water in weakly basic to basic solutions.^{10–16} While these materials are still outperformed by the state-of-the-art catalysts, the non-toxic nature, ease of scale-up and natural abundance of copper justify pursuing studies on rationally designed copper oxide electrodes.¹⁷ Given the importance of the dimensionality of these materials in determining their properties such as shortened ion diffusion pathways and increased electrochemically active areas,¹⁸ the synthesis of CuO with nanostructure and tailor-made morphology has attracted huge attention from researchers. To date, various synthesis routes such as thermal evaporation,¹⁹ microwave-assisted synthesis,²⁰ spray pyrolysis,^{21,22} solvothermal²³ and electrodeposition^{24,25} have been used to fabricate shape and

size-controlled CuO nanostructures. All these methods have their own drawbacks along with some other issues attached, *e.g.* being tedious, time-consuming and energy-intensive,^{26,27} involving costly raw materials, and requiring the indispensable presence of surfactants,^{23,28} toxic solvents^{29,30} or hard templates,^{1,31–33} thereby greatly hindering their mass-scale production and applications. For instance, Chang *et al.* synthesized CuO nanocrystallites by a solvothermal method between 140 and 180 °C for 20–40 h in highly toxic *N,N*-dimethylformamide solvent,³⁴ whereas Yu *et al.*³⁵ spent two weeks for the preparation of CuO nanoflowers. Huang *et al.* synthesized CuO nanorods by thermal evaporation of copper foil in an oxygen-rich environment at high temperatures ranging from 300 to 900 °C.¹⁹ When economic concerns are taken into account, electrodeposition has stood out as a well-suited route for obtaining nanostructures, mainly owing to its advantages of rapid deposition rates, cost-effectiveness, relatively low energy and space requirements.^{25,36} The key advantage is believed to be the controllability of the growth rate by monitoring various deposition parameters including pH conditions, bath temperature or external bias.^{37,38} Particularly, in the electrochemical growth of metal hydroxide or metal oxide nanostructures, the phase purity, crystalline nature, and porosity depend on the electrodeposition conditions.^{39–41} Although there are many research papers that have been published on the electrodeposition of CuO,^{37,42–44} little attention has been

Department of Chemical Engineering, National Taiwan University of Science and Technology, Taipei-106, Taiwan. E-mail: cychiang@mail.ntust.edu.tw;
Fax: +886-2-2737-6641; Tel: +886-2-2737-6641

† Electronic supplementary information (ESI) available. See DOI: 10.1039/C9DT04626G

paid to the nature of the Cu^{2+} precursor and the supporting electrolyte which can open up new possibilities for understanding the growth mechanism. Inspired by the above facts, in this work, we took advantage of flexible electrodeposition to investigate how the anion incorporation affected the structural morphology of copper layered hydroxyl salts and how it can influence the morphology and crystallinity of CuO . More specifically, probably the first on the subject, the possible origin of the significant differences in the morphology and dimensions of CuO as a function of the electrolyte composition was discussed. The correlation between the physico-chemical properties, surface morphology and electrochemical behavior of CuO samples was also established.

Experimental

Synthesis of copper layered hydroxide salts and their conversion into oxides

The methodology employed to synthesize nanostructured cupric oxides relies on the electrodeposition of copper layered hydroxide salts (Cu-LHSs) according to the work reported by Choi *et al.* with a slight modification⁴⁵ followed by thermal treatment as proposed by Chiang *et al.*⁴⁶ It is worth noting that in order to study the capability of copper oxide nanostructures in photoelectrochemical (PEC) water oxidation, a Cu-LHS was deposited on a bismuth vanadate (denoted as BVO) thin film photoanode. The typical fabrication procedure of spin-coated BVO was introduced in our previously reported study⁴⁷ and is also provided in ESI.† Various Cu-LHS films (denoted as Cu-LHS/X, where X indicates the anion) were deposited using Cu^{2+} solutions containing *p*-benzoquinone and their corresponding anions that were incorporated into the Cu-LHS structure. The anions were provided by a copper salt and a supporting electrolyte. Therefore, the types of copper salts and supporting electrolytes were changed based on the target formula of the Cu-LHS. For example, to prepare Cu-LHS/N, 20 mM $\text{Cu}(\text{NO}_3)_2$ and 100 mM NaNO_3 were used as the Cu^{2+} source and the supporting electrolyte, respectively. In the same manner, CuSO_4 and Na_2SO_4 were used as the Cu source and the supporting electrolyte to produce Cu-LHS/S. The cathodic electrodeposition was carried out at -0.1 V *vs.* Ag/AgCl at room temperature to pass a charge density of 40 mC cm^{-2} . This potential was chosen because it allows the sufficient *p*-benzoquinone reduction current while avoiding the reduction of Cu^{2+} to Cu^{1+} .

Upon the electrodeposition process, the prepared Cu-LHS nanostructures were heated to $400\text{ }^\circ\text{C}$ at a heating rate of $2\text{ }^\circ\text{C min}^{-1}$ in air by using a muffle furnace and calcination of the nanostructures was carried out for 1 h.

Materials characterization

X-ray diffraction (XRD) patterns were recorded on a Bruker D8 X-ray diffractometer with a rotatory anode in the 2θ range from 10° to 70° using 6° min^{-1} as step scan. High-resolution X-ray photoelectron spectra (XPS) were recorded using $\text{K}\alpha$ radiation

(XPS, Thermo VG ESCALAB250). Surface morphology was determined using a dual-beam focused ion beam scanning electron microscope (FEI Quanta 3D FEG, USA). Transmission electron microscopy (TEM) and high-resolution transmission electron microscopy (HR-TEM) images were obtained using a TECNAI G2 F20 TEM operating at 200 kV. The catalyst sample was removed from the substrate by sonication in absolute ethanol, and a drop of the mixture was dried on a copper grid. The optical bandgap was estimated from UV-Vis diffuse reflectance spectroscopic studies using a UV-Vis spectrophotometer (V650, Jasco) with FTO as the reference.

Raman spectroscopy was performed on a confocal Raman microscope system (MRID, Protrustech, Taiwan). A solid-state laser ($\lambda = 532\text{ nm}$) was used as the excitation source. To prevent degradation, the exposure time was set at 3 seconds with 10 accumulations. A $50\times$ objective lens was used and the measurement was carried out at room temperature and under dark conditions. Before the measurement, the Raman band of a silicon wafer at 520 cm^{-1} was used as the standard reference to calibrate the spectrometer.

All photoluminescence (PL) and time-resolved photoluminescence (TR-PL) lifetime measurements were performed using an integrated spectrometer (MRID, ProTrusTech Co., Taiwan) with a 405 nm laser as the excitation source. Nanosecond time-resolved photoluminescence (TR-PL) spectroscopy was conducted by the time-correlated single-photon counting (TCSPC) technique along with an instrument response function of 200 ps pulse duration and a repetition rate of 20 MHz. The deconvolution of the PL decay was performed using a biexponential decay function to deduce the time constant (refer ESI† for detailed calculations).

Photoelectrochemical measurements

The photoelectrochemical properties of the as-prepared electrode samples were examined in a 0.1 M borate aqueous solution (pH 9.4), using a potentiostat (Autolab PGSTAT302N, Metrohm, Switzerland) and a sunlight simulator (Model 66905, Newport) equipped with an AM 1.5G filter. The illuminating light intensity measured using a thermopile detector (Newport) was 100 mW cm^{-2} . Fabricated photoelectrodes were used as working electrodes. Pt mesh ($2.5\text{ cm} \times 2.5\text{ cm}$) was used as the counter electrode, while an Ag/AgCl (3 M KCl) electrode was used as the reference electrode. The photocurrent was measured by linear sweep voltammetry with a scan rate of 10 mV s^{-1} . The data were collected by back-illumination to minimize competitive absorption from the catalyst layer. The potential measured *vs.* the Ag/AgCl electrode was converted to the reversible hydrogen electrode potential using the Nernst equation. For calculating the charge injection efficiency, the photocurrent was measured by using 0.1 M Na_2SO_4 as the hole scavenger; the ratio of the photocurrents with and without the hole scavenger gave the charge injection efficiency of the photoanode. Chopped-light amperometric $J-t$ measurements were performed at an applied potential of 1.23 V *vs.* RHE under chopped light irradiation (light on/off cycle: 10 s).

Incident photon-to-current conversion efficiencies (IPCEs) were obtained by collecting the photocurrent recorded under monochromatic light irradiation (Oriel Cornerstone 130, Newport) using the same three-electrode setup as described above. The light power for each wavelength was measured using an optical power meter (Model 843R, Newport).

Impedance data were collected between 10^{-1} and 10^5 Hz using 10 mV amplitude voltage perturbation and analyzed by using Nova software (Metrohm). Mott–Schottky (M–S) plots were obtained in borate solution (pH 9.4) in the dark at a frequency of 1 kHz and a scan rate of 10 mV s $^{-1}$.

The amounts of oxygen and hydrogen were detected using a gas chromatograph (YL6500GC, Young Lin Instrument Co., Korea) with a thermal conductivity detector every 20 min. The faradaic efficiency was calculated according to the charge passed and the amount of O₂ evolved. For the ease of calculation, constant current density (0.5 mA cm $^{-2}$) was applied.

Results and discussion

Crystal structure investigation

The compositions and morphologies of Cu-LHS/X and CuO-X (where X indicates the anion) electrodes were characterized by a series of techniques. Crystal structural changes of Cu-LHS and CuO products were first examined by XRD. As shown in Fig. S1,[†] the XRD peaks of bare BVO can be indexed to the characteristic peaks of monoclinic bismuth vanadate (JCPDS 14-0688), while the diffraction peaks of annealed BVO/Cu-LHS precursor films deposited with NO₃⁻ and SO₄²⁻ can be indexed to copper nitrate hydroxide (JCPDS 05-0014) and copper sulfate hydroxide (JCPDS 43-1458). The large size of the SO₄²⁻ ion distorts the layers in the LHS product more, resulting in the broadening of the XRD peaks. As shown in Fig. 1, after heating at 400 °C in air, the Cu-LHS/N precursor samples entirely transformed to polycrystalline monoclinic CuO with major diffraction peaks at 35.54° and 38.60° corresponding to (002) and (111), respectively (JCPDS 89-5895). Irrespective of the deposition solution, no impurity phases such as Cu metal, Cu₂O or residual Cu(OH)₂ were observed, indirectly indicating that Cu-LHS could be transformed to CuO through calcination. Unfortunately, typical characteristic diffraction peaks of CuO-S were not observed evidently, which is a signature of lower crystallinity.

The Raman spectra of as-fabricated samples were also recorded to further ensure the phase of the products, detect the existence of unintended phases such as Cu₂O or Cu(OH)₂, and indicate the crystallinity of the product. The Raman spectra of BVO, BVO/CuO-S and BVO/CuO-N in the range of 150–1000 cm $^{-1}$ are shown in Fig. 1(b). At first, the results showed good agreement with previous reports on scheelite monoclinic BiVO₄ that has vibrational bands at about 211.8, 322.9, 367.8, 710.4 and 825 cm $^{-1}$. The Raman spectra of BVO/CuO-S and BVO/CuO-N showed an additional peak at 285.9 cm $^{-1}$ as compared with that of pure BVO, which can be attributed to the vibration mode of CuO.^{48,49} The absence of

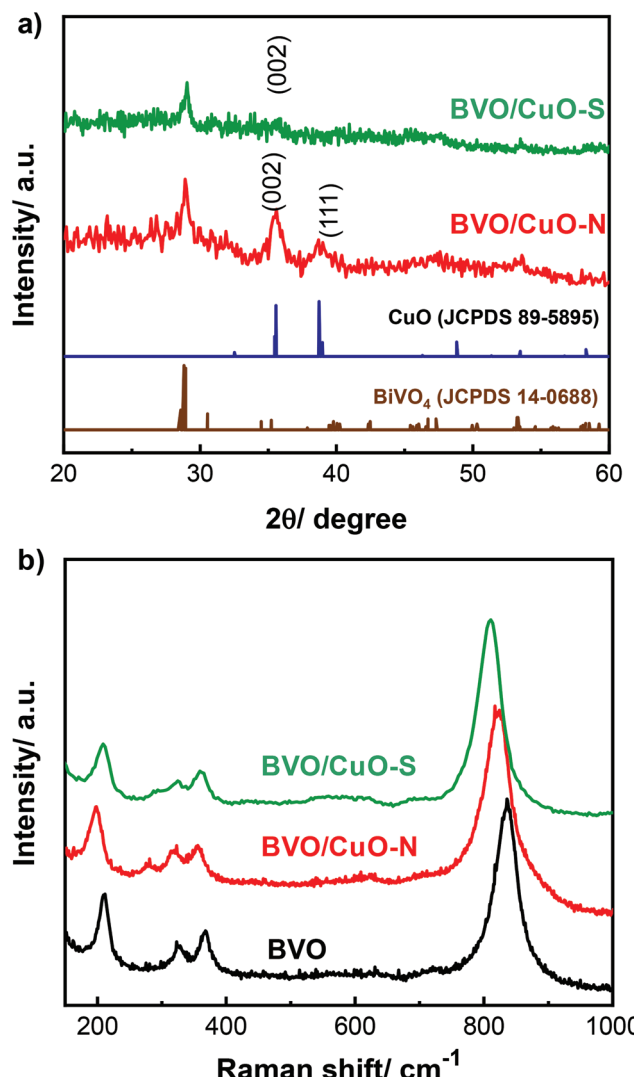


Fig. 1 XRD patterns (a) and Raman spectra (b) of BVO/CuO-S and BVO/CuO-N.

any Raman bands of copper hydroxides for BVO/CuO samples indicated the complete conversion of the Cu-LHS into CuO after thermal treatment, consistent with XRD results.

The surface chemical composition of the as-prepared Cu-LHS and its corresponding oxides was characterized using XPS, and all XPS data were calibrated with the carbon 1s peak at 284.8 eV. Fig. S2(a and b)[†] shows the high-resolution Cu 2p peak of the sample before and after thermal treatment. Both samples displayed characteristic peaks positioned at 933.6 eV and 953.9 eV respectively, which can be ascribed to Cu 2p_{3/2} and Cu 2p_{1/2}. Additional shake-up peaks (denoted as “sat.”) were also detected with a binding energy of ~10 eV higher than that of the main Cu 2p_{3/2} and Cu 2p_{1/2} peaks, due to the existence of an unfilled Cu 3d⁹ shell.⁵⁰ This confirms that only Cu²⁺ (neither Cu⁺ nor Cu⁰ with a binding energy of ca. 932.8 eV) existed on the surface of the fabricated sample.⁵¹ To study the variation of the OH⁻ bond on the surface before and after thermal treatment, the O 1s core level was also analyzed. As

can be seen in Fig. S2(c),[†] the O 1s core level of the Cu-LHS can be deconvoluted into four components at 528.2, 530.7, 531.9 and 533 eV which can be attributed to oxygen in the lattice (BVO underneath), the nitrate group, hydroxyl groups and absorbed water on the surface, respectively. The first component at 528.3 eV can be assigned to the M–O bonding in metal oxides from BVO underneath. The 530.7 eV peak corresponded to the N–O bonding from the nitrate group. The major peak located at 531.9 eV should be attributed to O in the hydroxyl of LHS, while a shoulder-like feature at 533 eV can be attributed to surface-bound hydroxide species that originates from the adsorbed H₂O molecules on the surface.^{13,52,53} After annealing, the decrease in peak intensity at 931.9 eV indicates that the Cu-LHS was decomposed and transformed to CuO (Fig. S2d[†]). As a result, XPS results coincided with the above XRD and Raman results, confirming that the Cu-LHS has been completely converted to CuO.

Morphological regulation of Cu-LHS and CuO nanostructures

The morphology of the Cu-LHS and CuO samples on BVO was first observed by SEM as depicted in Fig. S3[†] and Fig. 2. The bird-eye view SEM images of BVO (Fig. S3[†]) showed a relatively densely packed BVO film (thickness 200 nm, grain size 100–200 nm). Fig. 2 shows the morphological evolution of Cu-LHS nanostructures obtained in nitrate and sulfate media, respectively. As shown in Fig. 2a, using nitrate as the anion source can generate a layer composed of thin nanosheets that had a typical length of 1 μm and width of 10–20 nm. When sulfate was used as the anion, irregular nanoplates were observed but the homogeneity of the film was lower (Fig. 2b). The main difference between the two cases with different anions in the electrodeposition solution lies mainly in the size of the Cu-LHS crystal. The exact function of these anions during the growth of the LHS will be discussed later on.

Upon annealing at 400 °C, it is found that the surface morphology of the respective Cu-LHS/N precursor films was very

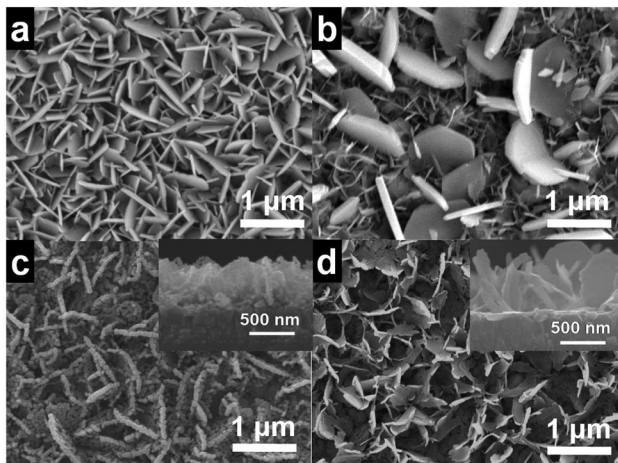


Fig. 2 SEM images of Cu-LHS/N (a), Cu-LHS/S (b), CuO-N (c) and CuO-S (d). The insets show the corresponding cross-sectional images.

well transformed into the final CuO products which maintained the size and shape of the Cu-LHS nanosheet precursor to some extent while generating porous structures. On the other hand, the thermal treatment of Cu-LHS/S resulted in the formation of CuO with relatively similar morphologies to its hydroxide precursors. In addition, EDS elemental mapping unambiguously confirmed the presence of Cu and O (with partial contribution from BVO underneath), as presented in Fig. S4 and S5.[†]

The microstructures of the as-obtained Cu-LHS and derived-CuO were further investigated by TEM and HRTEM characterization as shown in Fig. 3. The porous leaf-like nanosheet morphology can be clearly observed for the BVO/CuO-N sample composed of many interconnected nanoparticles with sizes of 20–30 nm. These nanoparticles were interconnected to form porous agglomerated microstructures with randomly distributed irregular pores (Fig. 3a), consistent with SEM observations. As for BVO/CuO-S, the sheet-like structure of hydroxides was well-preserved, albeit with some tiny pores being generated (Fig. 3b). In addition, the clear lattice images in Fig. 3c show that the BVO/CuO-N nanosheets were well crystallized. The lattice fringes with an interplanar spacing of 2.52 Å correspond to the (002) planes of the monoclinic CuO phase. Meanwhile, BVO/CuO-S nanosheets seemed to have poor crystallinity as evidenced by the absence of lattice fringes (Fig. 3d). The preceding results clearly showed the distinct influence of different intercalating anions on the morphologies and crystallinity of Cu-LHS and CuO nanostructures. Apparently, the change of the nature of the copper precursor and supporting electrolyte seems to be an effective way to

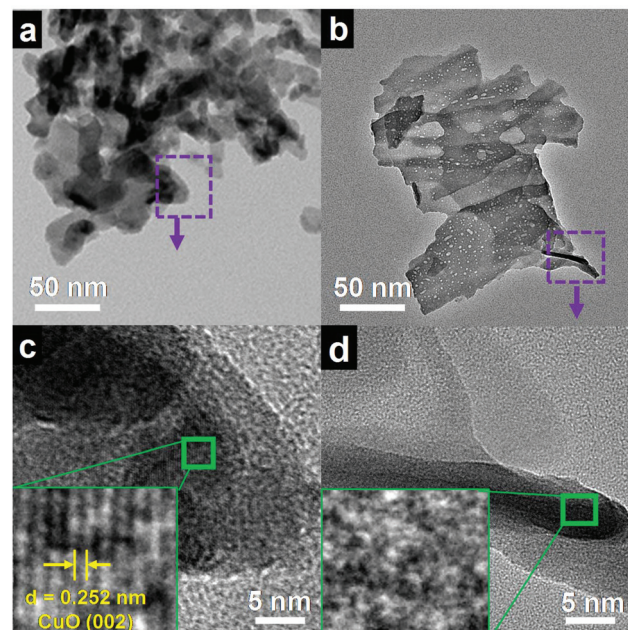


Fig. 3 TEM images of CuO-N (a), CuO-S (b) and HR-TEM images of CuO-N (c) and CuO-S (d). The insets show the corresponding enlarged images.

modulate the size and deposition rate during electrodeposition without depositing undesired species.

Growth mechanism of CuO with various metal salt anions

The morphological distinction between nitrate and sulfate systems appears to originate from the morphology of Cu-LHS films, which were used as precursors for CuO preparation. Therefore, the growth mechanism of the Cu-LHS with various metal salt anions was discussed. First, in order to help the readers gain knowledge of the role of charge-balancing anions in determining the morphology and crystal structure of the LHS, it is necessary to briefly discuss the structural aspects of the LHS. The basic features of the LHS structure involve positively charged brucite-like layers, with the general formula $M^{2+}(OH)_{2-x}(A^{m-})_{x/m} \cdot nH_2O$, where M^{2+} is the metal cation (e.g. Mg^{2+} , Ni^{2+} , Cd^{2+} , Co^{2+} , Cu^{2+}) and A^{m-} is the counter ion. It is known that the layered structure of the Cu-LHS is favorable for the formation of 2D sheet-like morphology.

At a certain external bias, hydroxide ions were generated on the working electrode (WE) by reducing *p*-benzoquinone, resulting in the elevation of the local pH at the WE surface. Consequently, Cu^{2+} reacted with OH^- and charge-balancing anions to produce primary crystal nuclei on the WE. It has been proposed that the change in particle sizes of the deposits can be explained by the difference in the nucleation and growth rates, depending on the nature of the electrolyte used.⁵⁴ The interaction between the cation and anion is believed to play an important role in the regulation of crystal growth of the LHS. Thus, the ionic strength (I) and activity (γ) of ions in chemical reactions should be considered in measuring the interaction between positive and negative ions. In this study, I was calculated to be 0.16 for the nitrate system and 0.38 mol L⁻¹ for the sulfate system. This indicated that the activity of nitrate in the chemical reaction and the degree of dissociation of nitrate in aqueous solution are higher than those of sulfate. A higher activity can promote homogeneous nucleation and thus generate additional small nuclei.⁵⁵ On the other hand, due to the weaker electrostatic bonding strength of NO_3^- than that of SO_4^{2-} , it is difficult for the primary nuclei in the nitrate system to grow into large sizes.⁵⁵ Plenty of small nuclei allowed the well-defined hexagonal LHS with relatively small and thin nanocrystals to develop on the surface of BVO in the nitrate system, whereas larger nuclei and comparatively thicker LHS nanocrystals were formed for the sulfate system.

In order to obtain further information regarding the growth rate of the deposits obtained in different anion media, the time evolution of current during the electrodeposition was recorded and is shown in Fig. S6.† As can be seen, in the current–time ($I-t$) curves generated in nitrate and sulfate media, a lower current value and a more slow steady-state were reached in sulfate, implying that greater energy is needed for the nucleation of the new phase.⁵⁴ Thus, it appears that the Cu-LHS formed and grew slowly in the presence of sulfate. This allowed sufficient time for maximal particle growth, resulting in the co-existence of small nanosheets and larger platelets. In contrast, in nitrate media, particle nucleation is

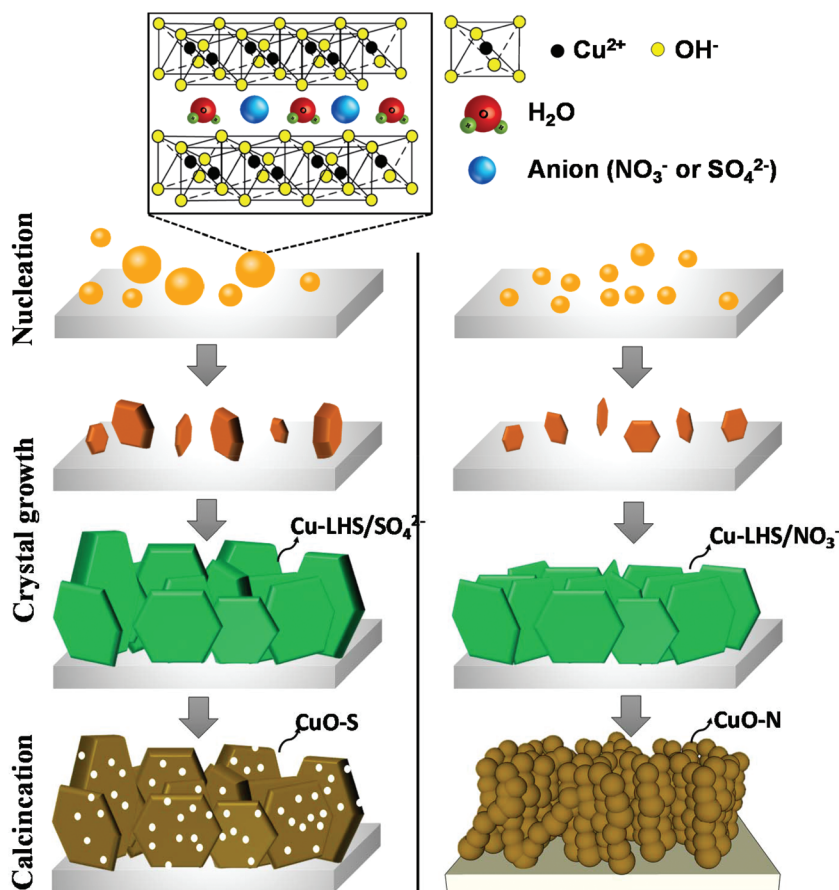
quicker, allowing the formation of smaller particles and agglomerates arranged mainly in the nanosheet array. During the thermal conversion of Cu-LHS to CuO, Cu-LHS layers act as a template for the formation of CuO nanoparticles. As illustrated in Scheme 1, the release of water molecules and intercalation anions during the annealing treatment possibly resulted in the porous structure of CuO.⁵⁶ As a result, the CuO films made from Cu-LHS films have unique nanostructures with high surface areas. Such nanostructured CuO films hold great promise for (photo)electrochemical applications where the surface area and the particle size play critical roles in electron–hole separation. Unlike the conventional nanostructures, the electrons in the 2D porous CuO nanosheet electrode can be transported between the interconnected nanoparticles.⁵⁷ To this end, it is reasonable to say that the anions have adequate indirect control over the porosity of CuO.

Evaluation of photoelectrochemical performance

The catalytic activity of as-prepared BVO/CuO-S and BVO/CuO-N films as photoanodes was investigated in PEC water splitting under standard simulated AM 1.5G irradiation in a 0.1 M NaBi electrolyte. The PEC measurement was conducted under back illumination (FTO side illumination). As shown in Fig. 4, the photocurrent density (J) was highly enhanced after compositing with CuO-S or CuO-N, achieving a J of 0.7 and 0.9 mA cm⁻² at 1.23 V vs. RHE, respectively. This was 40% (for CuO-S) and 80% (for CuO-N) higher than that of bare BVO. Apart from the photocurrent improvement, the onset potential was also estimated by the Butler method.⁵⁸ As shown in Fig. 4b, both BVO/CuO-S and BVO/CuO-N separately revealed cathodic shifts of 180 mV and 280 mV in terms of the onset potential, implying a positive catalytic water oxidation effect of CuO on BVO.

Given that the annealing step may also lead to a considerable change in the surface area of the resultant CuO product,⁶ the electrochemical surface area (ECSA) was further evaluated based on the double-layer capacitance (C_{dl}) of the catalysts. The C_{dl} of BVO/CuO-S and of BVO/CuO-N were obtained according to the CV plots recorded at different scan rates in the range of 4–12 mV s⁻¹ in the non-faradaic reaction range (0.09–0.19 V vs. Ag/AgCl). As shown in Fig. S8,† the C_{dl} of BVO/CuO-N was about 10 mF cm⁻², whereas the C_{dl} of BVO/CuO-S was only 7 mF cm⁻². Because the C_{dl} and electrochemical surface area are proportional to the active surface of materials,⁵⁹ it is reasonable to conclude that CuO-N samples provide a large active surface area that benefits from their higher porosity. Moreover, the nanostructured CuO-N films produced in this study are unique compared to the previously reported morphologies of directly electrodeposited CuO films, which typically resulted in dense, compact, featureless films.^{60–63}

To illustrate the interfacial coupling effect involved in the BVO/CuO-N photoanode, the optical properties of as-prepared photoanodes were investigated. Diffuse reflectance UV-visible spectra were first collected for BVO and BVO/CuO-N photoanodes to understand the influence of the heterostructure on



Scheme 1 Illustration of the transformation process from the Cu-LHS to porous CuO nanosheets.

Published on 22 January 2020. Downloaded on 2/14/2020 4:20:53 AM.

light-harvesting capability. As demonstrated in Fig. S9,† the absorption edge of BVO/CuO was extended compared to pristine BVO, which implies that the BVO/CuO-N photoanode has better visible light absorption capacity. Photoluminescence (PL) spectroscopy, which can be regarded as an effective approach to understand the separation efficiency of the photo-generated carriers, was performed at room temperature and the results are shown in Fig. 5. Generally, lower intensities in the emission spectra of the sample indicate a higher charge separation probability, thus leading to an enhanced photocatalytic activity.⁶⁴ The PL spectrum of pure BVO showed a strong emission peak at around 530 nm along with a broad peak centered at 575 nm. The peak at 530 nm was attributed to the charge-transfer transition between vanadium 3d and oxygen 2p orbitals in VO_4^{3-} and the peak at 575 nm corresponds to the charge transfer involving Bi and V centers.⁶⁵ The results presented in this paper are similar to those presented by Ma *et al.*, who observed two broad peaks at 510 and 560 nm.⁶⁵ It was observed that the PL emission intensity of BVO/CuO-N was slightly weakened compared with that of bare BVO, indicating that the combination of BVO and CuO would support better charge separation. By decorating CuO on BVO, the probability of recombination was suppressed and a higher charge carrier density was observed at the surface, indicating

higher visible light photocatalytic performance. For a deeper understanding of the thermodynamic charge carrier migration behavior, time-resolved photoluminescence (TRPL) measurement was conducted by the time-correlated single-photon counting (TCSPC) technique. The characteristic PL decay profiles were fitted by a biexponential function and are displayed in Fig. 5b. The time component parameters are summarized in Table S1 (details of the charge carrier lifetime calculation are provided in the ESI†). The average PL decay lifetime (t_{avg}) was 0.21 ns for BVO and 0.17 ns for BVO/CuO-N. The decreased lifetime indicated that the introduction of CuO as a cocatalyst effectively promoted the separation of electron–hole pairs compared to the bare BVO.⁶⁶

It has been demonstrated that both separation and transfer efficiencies of charge carriers within a photocatalyst are crucial to determine its photocatalytic activity. As such, the transient photocurrent response was applied to investigate the charge separation behavior of different samples. Fig. 6a illustrates the comparison of J – t curves of the BVO and BVO/CuO-N samples with several on–off cycles of intermittent irradiation. Observation of a small negative spike following light turn off in Fig. 6a is probably associated with the recombination at the interface due to incomplete physical contact between BVO and CuO layers. Given that the addition of an appropriate hole sca-

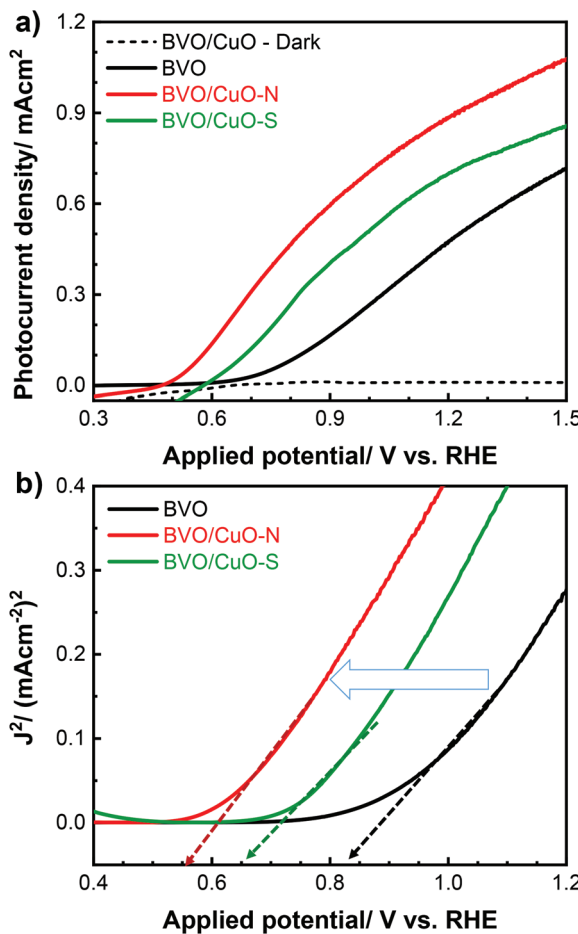


Fig. 4 (a) Photocurrent–potential curves and (b) corresponding Butler plots, in which the onset potential is defined for BVO, BVO/CuO–S and BVO/CuO–N under AM 1.5G irradiation.

venger could reveal the ultimate performance limit of photoanodes in the absence of surface electron–hole recombination, and thus PEC properties can be studied independently, we examined the photoelectrochemical properties of the as-obtained photoanodes in a hole scavenger containing solution (0.1 M NaBi–0.1 M Na_2SO_3). As an efficient hole scavenger, sulfite can be oxidized with favorable thermodynamics and kinetics, and thus the hole-transfer kinetics at the photoanode/electrolyte interface is generally negligible. As can be seen in Fig. 6b, the photocurrent of bare BVO for water oxidation was much lower than the photocurrent for sulfite oxidation, revealing that the majority of surface-reaching holes were lost for recombination on the BVO surface. In the meantime, when CuO was deposited on BVO for water oxidation, the J – V curve of BVO/CuO–N approached the sulfite oxidation curve, indicating that the presence of CuO can increase the rate of water oxidation and prevent the surface hole accumulation. Therefore, for direct comparison, the contribution of CuO was quantified on the basis of the injection efficiency, which represents the fraction of holes that reach the electrode/electrolyte interface and participate in water oxidation. The cal-

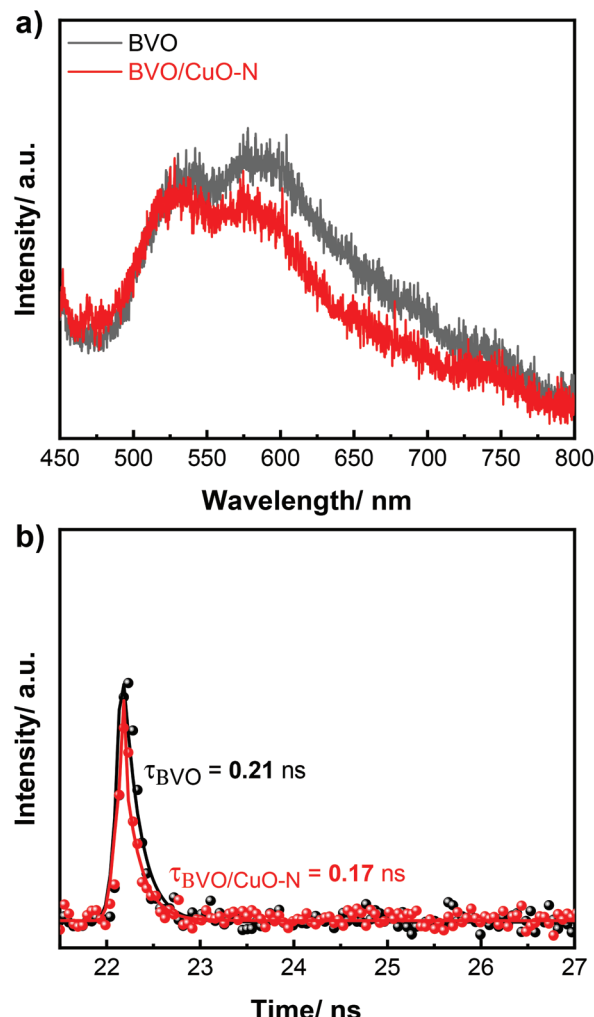


Fig. 5 (a) PL emission spectra of BVO and BVO/CuO–N (excitation wavelength of the PL measurements was 405 nm) and (b) time-resolved PL spectra recorded at the peak emission wavelength (530 nm).

culated result is shown in Fig. 6c. At 1.23 V vs. RHE, the $\eta_{\text{injection}}$ of BVO/CuO–N reached 65%, which is almost 2 times that of the BVO electrode, indicating that CuO coupling with BVO can improve the charge injection kinetics. However, it should be noted that the photocurrent of BVO/CuO–N was relatively lower than that of BVO for sulfite oxidation, indicating a possibility of partial photogenerated electron–hole pair recombination at the BVO/CuO–N interface. While the rate of holes entering the catalyst layer was higher than the rate of interfacial holes transferring for water oxidation, the holes could be accumulated in the catalyst layer as well as at the BVO/CuO–N interface, which resulted in the increase of electrons transferring from the conduction band of BVO to the catalyst layer for surface electron–hole pair recombination.⁶⁷ This suggests that there is still large room for further enhancing hole injection efficiency. Further insights into the role of CuO in modifying the properties of BVO photoanodes in the water splitting reaction are derived from the analysis of incident photon to current conversion efficiency (IPCE). As shown in Fig. 6d, the

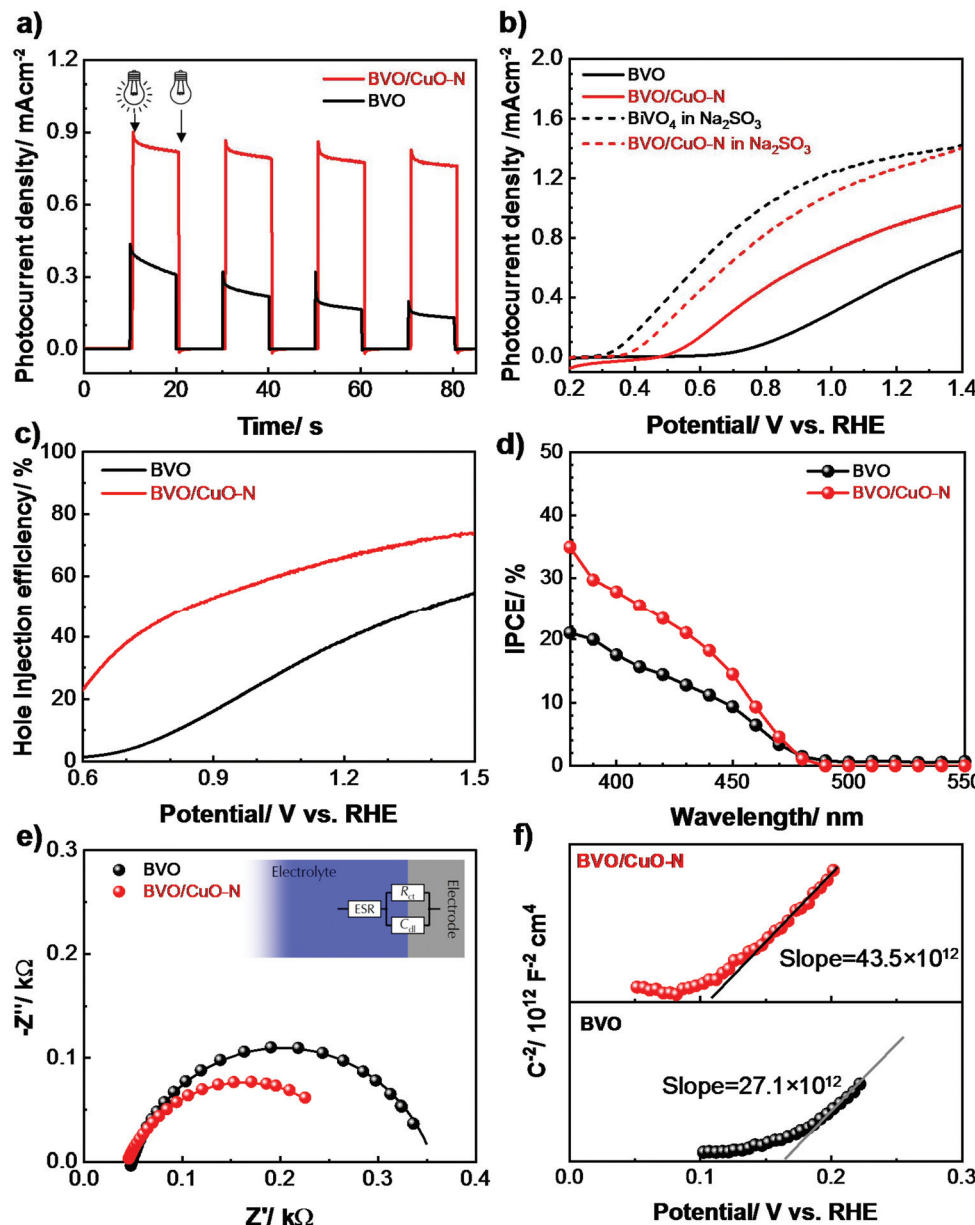


Fig. 6 (a) Transient photocurrent response of BVO and BVO/CuO-N at 1.23 V vs. RHE; (b) J – V curves of BVO and BVO/CuO-N with and without adding Na_2SO_3 ; (c) hole injection efficiencies; (d) IPCE spectra (e) Nyquist plot obtained at 1.23 V under AM 1.5G irradiation in borate buffer (pH 9.4) and (f) Mott–Schottky plots collected at a frequency of 1 kHz for BVO and BVO/CuO-N under dark conditions.

presence of CuO decorating BVO slightly increased the IPCE in the 350–450 nm spectral region, while it had no effect at higher wavelengths. This result suggested that only BVO acted as a photoresponsive material, while the slightly enhanced absorption in the visible light range caused by CuO did not contribute to the photocurrent.^{68–70}

The interfacial charge transfer properties of the electrodes were studied by electrochemical impedance spectroscopy (EIS) analysis over the frequency range of 10^5 Hz–0.01 Hz. The radius of the arc on the EIS Nyquist plot reflects the charge transfer kinetics during the photocatalytic process. Normally, a smaller semicircle radius of the Nyquist plot implies lower

charge transfer resistance, and thus a higher transfer rate of electron–hole pairs. As can be seen from Fig. 6e, the incorporation of CuO caused a significant decrease in the radius of the arc compared with the bare BVO under irradiation, suggesting that the deposition of CuO on the BVO surface facilitates the transfer of photo-induced electrons from the BVO surface to the electrolyte solution. The EIS results showed a clear appearance of easier electron–hole separation through the heterostructure which was also supported by photoluminescence spectroscopy and time-resolved spectroscopy. In addition, careful investigation of capacitance showed that double-layer capacitance was also increased to as much as 50% by CuO

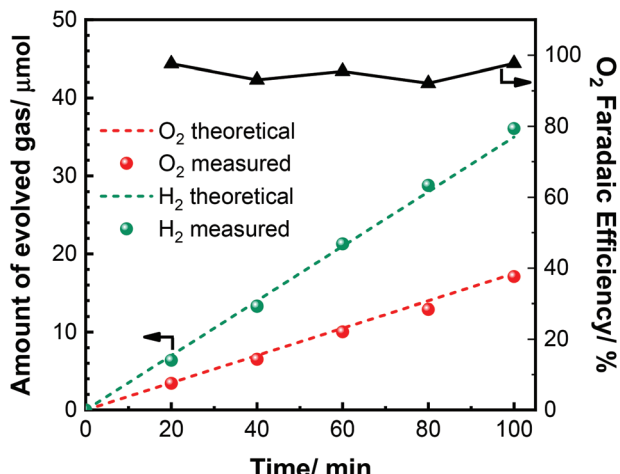


Fig. 7 Amount of evolved O₂ (red dot) and H₂ (blue triangle) produced by water oxidation for the BVO/CuO-N photoanode (1.5 cm × 1.5 cm) at a constant current of 0.5 mA cm⁻² in borate buffer. Red and blue dashed lines are the theoretical amounts of O₂ and H₂, respectively.

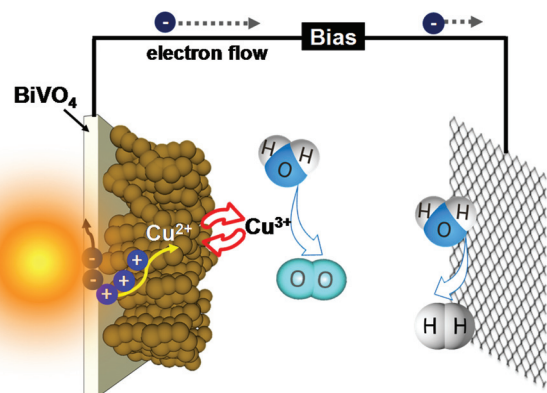


Fig. 8 Schematic representation of the integrated BVO/CuO photoanode architecture with directions of charge separation and transportation, together with the solar water oxidation mechanism.

deposits, owing to the rapid hole transfer which may charge CuO and may be maintained for a certain period of time.⁷¹ Impedance measurements conducted on BVO and BVO/CuO-N in a 0.1 M NaBi electrolyte in the dark allowed the construction of Mott-Schottky plots from which the flat-band potentials (V_{fb}) of the two materials were extrapolated from the x-axis intercept. Fig. 6(f) shows the Mott-Schottky plots of BVO and BVO/CuO-N electrodes measured at 1 kHz. Upon CuO modification, the flat band potential only shifted slightly negatively (~70 mV), indicating that CuO deposition does not induce a significant effect on band bending at the surface but mainly on the promotion of surface reaction kinetics. In addition, given that charge carrier density is inversely proportional to the slope in the plot of $1/C^2$ vs. potential, it is surprising that the Mott-Schottky slope of the modified sample is higher than that of the bare one. This may be due to the fact that the electrons and holes were trapped at the BVO and CuO

interface when no light was irradiated.⁷² Taken together, it is reasonable to conclude that the possibility of forming a p-n junction between CuO and the semiconductor which could promote the charge separation can be ruled out. It is believed that it is more appropriate for CuO to act as a co-catalyst.

To confirm that the photocurrent enhancement in the BVO/CuO-N electrode is mainly associated with oxygen evolution, not with other side reactions, the gas products were quantitatively measured using gas chromatography. The gas evolution and faradaic efficiency (the detailed calculation is shown in the ES[†]) as a function of the irradiation time are shown in Fig. 7 and Fig. S10.[†] An overall OER faradaic efficiency of 84% and 95% was obtained for bare BVO and BVO/CuO-N, respectively. The faradaic loss could be ascribed to the unwanted side reactions occurring at the photoanode. These results indicated that CuO serving as a water oxidation catalyst can not only enhance the photocurrent but also selectively increase the water oxidation kinetics. To further explore the stability properties of the integrated photoanode, the morphological structure and chemical states of the BVO/CuO electrode before and after water oxidation were re-evaluated by SEM and high-resolution XPS (Fig. S11 and S12[†]). As shown in Fig. S11,[†] morphology of BVO/CuO-N was relatively well-preserved after PEC water splitting as expected from its high faradaic efficiency. High-resolution XPS of BVO/CuO-N samples after the water splitting process showed no obvious change in the relative intensities of all elements, suggesting the photostability of the electrode (Fig. S12[†]).

Combining the results presented above, a tentative mechanism of the OER on BVO/CuO-N is suggested and illustrated in Fig. 8. It is believed that the Cu-based nanomaterials may have the same catalytic mechanism for the OER, that is, the surface Cu^{II} is oxidized to highly valent Cu^{III}-O active species for a further OER process, as recently identified by means of in-operando Raman spectroscopy by Yeo and co-workers.⁷³ Taken together, we therefore propose that under solar irradiation, CuO can be charged by photogenerated holes from BVO, which could be further oxidized to a highly valent Cu-oxo active component for the OER. After oxygen liberation, the Cu-oxo species is restored to CuO.^{16,74} These Cu-oxo species further oxidized water for releasing oxygen and simultaneously restored CuO, which completed a catalytic cycle for the oxygen evolution. In the meantime, photogenerated electrons from BVO migrated to the counter electrode through an external circuit for the generation of hydrogen.

Conclusion

We have employed the benefits of the simple electrodeposition method to investigate the role of interlayer anions in the formation of copper layered hydroxyl salts and their corresponding oxides. Tuning of the morphology, size and uniformity of copper-based materials is accomplished by regulating the anionic species present in the electroplating solution. The hybrid photoelectrode fabricated by coupling porous CuO

nanosheets obtained in nitrate media with bismuth vanadate exhibited better photoelectrochemical water splitting activity compared to the bare BiVO_4 . The onset potential was found to be cathodically shifted by 180 mV, while the photocurrent experienced an approximately 2-fold enhancement. The unique nanostructures increased the surface area and shortened the distance that the photogenerated holes need to travel to reach the interface which can significantly reduce electron-hole recombination, thereby enhancing solar water splitting performance.

Conflicts of interest

There are no conflicts to declare.

Acknowledgements

This work was financially supported by the Young Scholar Fellowship Program by the Ministry of Science and Technology (MOST) in Taiwan, under Grant MOST108-2636-E-011-001 and MOST109-2636-E-011-001. The authors would like to express their gratitude to the National Taiwan University of Science and Technology for facility support.

References

- 1 G. S. Gund, D. P. Dubal, D. S. Dhawale, S. S. Shinde and C. D. Lokhande, *RSC Adv.*, 2013, **3**, 24099–24107.
- 2 G. Wang, J. Huang, S. Chen, Y. Gao and D. Cao, *J. Power Sources*, 2011, **196**, 5756–5760.
- 3 P. Arul and S. A. John, *J. Electroanal. Chem.*, 2017, **799**, 61–69.
- 4 S. Shahrokhian, R. Kohansal, M. Ghalkhani and M. K. Amini, *Electroanalysis*, 2015, **27**, 1989–1997.
- 5 X. Zhang, G. Wang, X. Liu, J. Wu, M. Li, J. Gu, H. Liu and B. Fang, *J. Phys. Chem. C*, 2008, **112**, 16845–16849.
- 6 Z. Deng, Z. Ma, Y. Li, Y. Li, L. Chen, X. Yang, H. E. Wang and B. L. Su, *Front. Chem.*, 2018, **6**, 428.
- 7 Z. Wang, Y. Zhang, H. Xiong, C. Qin, W. Zhao and X. Liu, *Sci. Rep.*, 2018, **8**, 6530.
- 8 C. Wang, Q. Li, F. Wang, G. Xia, R. Liu, D. Li, N. Li, J. S. Spendelow and G. Wu, *ACS Appl. Mater. Interfaces*, 2014, **6**, 1243–1250.
- 9 H. Yu, J. Yu, S. Liu and S. Mann, *Chem. Mater.*, 2007, **19**, 4327–4334.
- 10 T. N. Huan, G. Rousse, S. Zanna, I. T. Lucas, X. Xu, N. Menguy, V. Mougel and M. Fontecave, *Angew. Chem., Int. Ed.*, 2017, **56**, 4792–4796.
- 11 X. Liu, S. Cui, Z. Sun and P. Du, *Electrochim. Acta*, 2015, **160**, 202–208.
- 12 X. Liu, S. Cui, Z. Sun, Y. Ren, X. Zhang and P. Du, *J. Phys. Chem. C*, 2016, **120**, 831–840.
- 13 K. S. Joya and H. J. M. de Groot, *ACS Catal.*, 2016, **6**, 1768–1771.
- 14 J. Du, Z. Chen, S. Ye, B. J. Wiley and T. J. Meyer, *Angew. Chem., Int. Ed.*, 2015, **54**, 2073–2078.
- 15 N. Cheng, Y. Xue, Q. Liu, J. Tian, L. Zhang, A. M. Asiri and X. Sun, *Electrochim. Acta*, 2015, **163**, 102–106.
- 16 C. C. Hou, W. F. Fu and Y. Chen, *ChemSusChem*, 2016, **9**, 2069–2073.
- 17 S. Manna, K. Das and S. K. De, *ACS Appl. Mater. Interfaces*, 2010, **2**, 1536–1542.
- 18 J. Zhou, Y. Dou, A. Zhou, L. Shu, Y. Chen and J.-R. Li, *ACS Energy Lett.*, 2018, **3**, 1655–1661.
- 19 L. S. Huang, S. G. Yang, T. Li, B. X. Gu, Y. W. Du, Y. N. Lu and S. Z. Shi, *J. Cryst. Growth*, 2004, **260**, 130–135.
- 20 G. Qiu, S. Dharmarathna, Y. Zhang, N. Opembe, H. Huang and S. L. Suib, *J. Phys. Chem. C*, 2012, **116**, 468–477.
- 21 A. Moumen, B. Hartiti, P. Thevenin and M. Siadat, *Opt. Quantum Electron.*, 2017, **49**, 70.
- 22 C. Y. Chiang, K. Aroh and S. H. Ehrman, *Int. J. Hydrogen Energy*, 2012, **37**, 4871–4879.
- 23 Y. Zhang, S. Wang, X. Li, L. Chen, Y. Qian and Z. Zhang, *J. Cryst. Growth*, 2006, **291**, 196–201.
- 24 X. Liu, Z. Sun, S. Cui and P. Du, *Electrochim. Acta*, 2016, **187**, 381–388.
- 25 Y. Wang, T. Jiang, D. Meng, J. Yang, Y. Li, Q. Ma and J. Han, *Appl. Surf. Sci.*, 2014, **317**, 414–421.
- 26 G. G. Condorelli, G. Malandrino and I. L. Fragal, *Chem. Vap. Deposition*, 1999, **5**, 237–244.
- 27 D. Jia, J. Yu and X. Xia, *Chin. Sci. Bull.*, 1998, **43**, 571–573.
- 28 K. Borgohain, J. B. Singh, M. V. Rama Rao, T. Shripathi and S. Mahamuni, *Phys. Rev. B: Condens. Matter Mater. Phys.*, 2000, **61**, 11093–11096.
- 29 R. Vijaya Kumar, R. Elgamiel, Y. Diamant, A. Gedanken and J. Norwig, *Langmuir*, 2001, **17**, 1406–1410.
- 30 K. Borgohain, J. B. Singh, M. V. Rama Rao, T. Shripathi and S. Mahamuni, *Phys. Rev. B: Condens. Matter Mater. Phys.*, 2000, **61**, 11093–11096.
- 31 M. Aghayan, I. Hussainova, K. Kirakosyan and M. A. Rodríguez, *Mater. Chem. Phys.*, 2017, **192**, 138–146.
- 32 Y. Zou, Y. Li, Y. Guo, Q. Zhou and D. An, *Mater. Res. Bull.*, 2012, **47**, 3135–3140.
- 33 M. A. Kamyabi, N. Hajari, N. Babaei, M. Moharramnezhad and H. Yahiro, *J. Taiwan Inst. Chem. Eng.*, 2017, **81**, 21–30.
- 34 Y. Chang, J. J. Teo and H. C. Zeng, *Langmuir*, 2005, **21**, 1074–1079.
- 35 L. Yu, G. Zhang, Y. Wu, X. Bai and D. Guo, *J. Cryst. Growth*, 2008, **310**, 3125–3130.
- 36 R. Della Noce, S. Eugénio, T. M. Silva, M. J. Carmezim and M. F. Montemor, *RSC Adv.*, 2017, **7**, 32038–32043.
- 37 V. Dhanasekaran, T. Mahalingam, R. Chandramohan, J. K. Rhee and J. P. Chu, *Thin Solid Films*, 2012, **520**, 6608–6613.
- 38 M. J. Siegfried and K.-S. Choi, *J. Am. Chem. Soc.*, 2006, **128**, 10356–10357.
- 39 I. Udachyan, R. S. Vishwanath, C. S. P. Kumara and S. Kandaiah, *Int. J. Hydrogen Energy*, 2019, **44**, 7181–7193.
- 40 Z. Su, W. Zhou, F. Jiang and M. Hong, *J. Mater. Chem.*, 2012, **22**, 535–544.

41 H. C. Shin, J. Dong and M. Liu, *Adv. Mater.*, 2003, **15**, 1610–1614.

42 A. Roy, H. S. Jadhav, M. Cho and J. G. Seo, *J. Ind. Eng. Chem.*, 2019, **76**, 515–523.

43 A. Esmaeeli, A. Ghaffarinejad, A. Zahedi and O. Vahidi, *Sens. Actuators, B*, 2018, **266**, 294–301.

44 M. J. Siegfried and K.-S. Choi, *J. Am. Chem. Soc.*, 2006, **128**, 10356–10357.

45 A. C. Cardiel, K. J. McDonald and K. S. Choi, *Langmuir*, 2017, **33**, 9262–9270.

46 C. Y. Chiang, Y. Shin, K. Aroh and S. Ehrman, *Int. J. Hydrogen Energy*, 2012, **37**, 8232–8239.

47 B. E. Wu and C. Y. Chiang, *J. Taiwan Inst. Chem. Eng.*, 2017, **80**, 1014–1021.

48 D. Ren, J. Fong and B. S. Yeo, *Nat. Commun.*, 2018, **9**, 925.

49 M. Rashad, M. Rusing, G. Berth, K. Lischka and A. Pawlis, *J. Nanomater.*, 2013, **2013**, 6.

50 S. M. Pawar, B. S. Pawar, B. Hou, J. Kim, A. T. A. Ahmed, H. S. Chavan, Y. Jo, S. Cho, A. I. Inamdar, J. L. Gunjakar, H. Kim, S. Cha and H. Im, *J. Mater. Chem. A*, 2017, **5**, 12747–12751.

51 L. Zhang, Y. C. Zhu, Y.-Y. Liang, W.-W. Zhao, J. J. Xu and H. Y. Chen, *Anal. Chem.*, 2018, **90**, 5439–5444.

52 D. Xiong, Z. Du, H. Li, J. Xu, J. Li, X. Zhao and L. Liu, *ACS Sustainable Chem. Eng.*, 2019, **7**, 1493–1501.

53 A. C. Nwanya, D. Obi, K. I. Ozoemena, R. U. Osuji, C. Awada, A. Ruediger, M. Maaza, F. Rosei and F. I. Ezema, *Electrochim. Acta*, 2016, **198**, 220–230.

54 P. Montoya, T. Marín, A. Echavarría and J. A. Calderón, *Int. J. Electrochem. Sci.*, 2013, **8**, 12566–12579.

55 Q. Mei, W. Lv, M. Du and Q. Zheng, *RSC Adv.*, 2017, **7**, 46576–46588.

56 B. G. Ganga and P. N. Santhosh, *Mater. Lett.*, 2015, **138**, 113–115.

57 L. Li, G. Jiang, R. Sun and B. Cao, *New J. Chem.*, 2017, **41**, 15283–15288.

58 N. Guijarro, M. S. Prévot, X. Yu, X. A. Jeanbourquin, P. Bornoz, W. Bourée, M. Johnson, F. Le Formal and K. Sivila, *Adv. Energy Mater.*, 2016, **6**, 1501949.

59 T. T. Li, J. Qian and Y.-Q. Zheng, *RSC Adv.*, 2016, **6**, 77358–77365.

60 M. Izaki, M. Nagai, K. Maeda, F. B. Mohamad, K. Motomura, J. Sasano, T. Shinagawa and S. Watase, *J. Electrochem. Soc.*, 2011, **158**, D578–D584.

61 J. S. Sagu, T. A. N. Peiris and K. G. U. Wijayantha, *Electrochem. Commun.*, 2014, **42**, 68–71.

62 P. Poizot, C. J. Hung, M. P. Nikiforov, E. W. Bohannan and J. A. Switzer, *Electrochem. Solid-State Lett.*, 2003, **6**, C21–C25.

63 M. J. Siegfried and K.-S. Choi, *J. Electrochem. Soc.*, 2007, **154**, D674–D677.

64 M. Wang, W. Li, Y. Zhao, S. Gu, F. Wang, H. Li, X. Liu and C. Ren, *RSC Adv.*, 2016, **6**, 75482–75490.

65 D. K. Ma, M.-L. Guan, S.-S. Liu, Y.-Q. Zhang, C.-W. Zhang, Y.-X. He and S.-M. Huang, *Dalton Trans.*, 2012, **41**, 5581–5586.

66 D. Kim, Z. Zhang and K. Yong, *Nanoscale*, 2018, **10**, 20256–20265.

67 T. W. Kim and K. S. Choi, *Science*, 2014, **343**, 990–994.

68 J. A. Seabold and K.-S. Choi, *J. Am. Chem. Soc.*, 2012, **134**, 2186–2192.

69 T. G. Vo, Y. Tai and C. Y. Chiang, *J. Catal.*, 2019, **370**, 1–10.

70 Y. Huang, Y. Yu, Y. Xin, N. Meng, Y. Yu and B. Zhang, *Sci. China Mater.*, 2017, **60**, 193–207.

71 T. H. Jeon, W. Choi and H. Park, *Phys. Chem. Chem. Phys.*, 2011, **13**, 21392–21401.

72 J. Li, F. Meng, S. Suri, W. Ding, F. Huang and N. Wu, *Chem. Commun.*, 2012, **48**, 8213–8215.

73 Y. Deng, A. D. Handoko, Y. Du, S. Xi and B. S. Yeo, *ACS Catal.*, 2016, **6**, 2473–2481.

74 Q. Zhou, T. T. Li, J. Qian, Y. Hu, F. Guo and Y. Q. Zheng, *J. Mater. Chem. A*, 2018, **6**, 14431–14439.